



Virginia Commonwealth University  
VCU Scholars Compass

---

Chemistry Publications

Dept. of Chemistry

---

2020

## High-Pressure Infiltration–Expulsion of Aqueous NaCl in Planar Hydrophobic Nanopores

S. Zamfir

F. Moucka

D. Bratko

*Virginia Commonwealth University*, [dbratko@vcu.edu](mailto:dbratko@vcu.edu)

Follow this and additional works at: [https://scholarscompass.vcu.edu/chem\\_pubs](https://scholarscompass.vcu.edu/chem_pubs)

 Part of the [Chemistry Commons](#)

---

Downloaded from

[https://scholarscompass.vcu.edu/chem\\_pubs/102](https://scholarscompass.vcu.edu/chem_pubs/102)

This Article is brought to you for free and open access by the Dept. of Chemistry at VCU Scholars Compass. It has been accepted for inclusion in Chemistry Publications by an authorized administrator of VCU Scholars Compass. For more information, please contact [libcompass@vcu.edu](mailto:libcompass@vcu.edu).

# High Pressure Extrusion/Intrusion of Aqueous NaCl in Planar Hydrophobic Nanopores

Serban Zamfir<sup>1</sup>, Filip Moucka<sup>2</sup>, Dusan Bratko<sup>1,\*</sup>

<sup>1</sup>Department of Chemistry, Virginia Commonwealth University, Richmond, Virginia 23221, United States, and <sup>2</sup>Department of Physics, Faculty of Science, J. E. Purkyně University, 400 96 Ústí nad Labem, Czech Republic

(Aug 4, 2020)

## Abstract

Pressure-driven permeation of water in a poorly wettable material results in a conversion of mechanical work into surface free energy representing a new form of energy storage, or absorption. When water is replaced by a concentrated electrolyte solution, the storage capacity of a nanoporous medium becomes comparable to high-end supercapacitors. The addition of salt can also reduce the hysteresis of the infiltration/expulsion cycle. Our molecular simulations provide a theoretical perspective into the mechanisms involved in the process, and underlying structures and interactions in compressed nanoconfined solutions. Specifically, we consider aqueous NaCl in planar confinements of widths of 1.0 nm and 1.64 nm and pressures of up to 3 kbar. Open ensemble Monte Carlo simulations utilizing fractional exchanges of molecules for efficient additions/removal of ions have been utilized in conjunction with pressure-dependent chemical potentials to model bulk phases under pressure. Confinements open to these pressurized bulk, aqueous electrolyte phases show reversibility at narrow pore sizes, consistent with experiment, as well as strong hysteresis at both pore size. The addition of salt results in significant increases in the solid/liquid interfacial tension in narrower pores and associated infiltration and expulsion pressures. These changes are consistent with strong desalination effects at the lower pore size observed irrespective of external pressure and initial concentration.

---

\* Email: [dbratko@vcu.edu](mailto:dbratko@vcu.edu)

## I. INTRODUCTION

Compression of water in strongly hydrophobic nanopores has been established as a viable mechanism of energy storage underlying the function of liquid springs and shock absorbers.<sup>1</sup> According to conventional continuum estimates, the stored energy density can be approximated by the product of specific area and the wetting free energy,  $\Delta\gamma$ . In an ideal case, this energy equals the work  $P_{in}\Delta V$  recovered upon expulsion, where  $P_{in}$  is the intrusion pressure  $P_{in} \sim \frac{2\Delta\gamma}{d_z}$ ,  $d_z \propto a^{-1}$  is the effective pore diameter and  $a$  is specific area. Nanoporous hydrophobic materials such as zeolites, typically composed of alumina and silica, have long been studied as suitable media for the storage of surface energy. Metal-organic frameworks represent a highly promising alternative<sup>2</sup>. The attainable density of stored energy has been shown to increase when water is replaced by electrolyte solution but the gain also depends on the type of zeolite.<sup>3-10</sup> Saline-filled zeolites with experimental pore sizes of 1.0 nm or lower have been shown to have high energy density capabilities that are in the range of 0.1-1.0 Jg<sup>-1</sup> which is comparable to supercapacitors.<sup>8-9, 11</sup> The conversion between mechanical work delivered upon compression and surface free energy is, however, not always reversible. The expulsion of solution following a release of the pressure can follow three distinct behaviors: full energy recovery (liquid spring), partial energy recovery (shock-absorber), or no energy recovery (bumper).<sup>8, 12</sup> In addition to the properties of the selected porous material, the outcome can depend on the composition/concentration of the electrolyte solution. Increasing the concentration of the solution, or ion type can, in some cases, shift the system from bumper to shock-absorber or liquid spring behavior.<sup>13</sup> Molecular mechanisms behind the observed salt effects are only partly understood and have so far not been accessible to experiment. We strive to uncover generic features of nanoconfined electrolytes and their response to pressure variation using molecular simulations. To this end, we study the mechanisms, structural

changes, and thermodynamic driving forces controlling water and electrolyte intrusion/extrusion into/from a nanopore.

We use the Grand Canonical Monte Carlo (GCMC) simulation which is typically better suited for studies of equilibrium properties in open system than Molecular Dynamics (MD) simulations<sup>14</sup>. The focus of this study is on the intrusion/extrusion of concentrated NaCl solution into nanopores of size 1.0 nm and 1.64 nm. Alternative choices of electrolyte, such as LiCl favored in recent experiments because of its extreme solubility, are at this time not feasible because of scarce experimental data for the chemical potential, the drive to mix in a GCMC simulation.<sup>15</sup> Experimental bulk phase studies conducted by Adams<sup>16</sup> considered the entire range of accessible NaCl concentrations from ambient conditions to extreme pressures to determine partial molar volumes for each species. In turn, a chemical potential over a range of pressures can be calculated as described in more detail in section III.A of this work. Our study covers the experimentally relevant pressure range from 1 bar to 3000 bar for bulk electrolyte molalities 5.70 mol kg<sup>-1</sup>, 4.28 mol kg<sup>-1</sup>, 3.02 mol kg<sup>-1</sup>, and 0 (neat water).

Consistent with previous works<sup>17-20</sup>, our results show that only the narrow pore size can secure an intrusion reversal upon decompression. Moreover, we observe strong hysteresis in all cases. Simulation results establish an enhanced energy storage capacity with decreasing pore size and higher salt concentration as narrower pores act increasingly more hydrophobic. The salt contribution to this increase proves much more pronounced in narrow pores. This is consistent with significantly stronger, although incomplete, desalination in the narrower pore. The salt exclusion is not ameliorated with increased pressures and can be expected to play an even more important role with highly soluble salts like LiCl. All the more prominent salt effects leading to improved reversibility of the infiltration/expulsion cycle observed in some experiments, can be

rationalized in terms of near-complete ion defiltration<sup>21</sup> due to the narrowed window size of pore cages, a medium-specific feature to be addressed in a separate study.

## II. METHODS

**A. Models.** To study the intrusion and extrusion of aqueous NaCl in confinement we use classical molecular simulations with hydrophobic walls of separation  $d_z$  of 1.0 nm and 1.64 nm. The narrow wall separation of 1.0 nm was chosen based on relevant experimental studies<sup>3-5, 9, 22</sup> while the larger pore was chosen to be just above the kinetic threshold with respect to capillary evaporation<sup>17-18, 23-29</sup> in neat water and ambient conditions. With these choices, the solution-accessible width  $d_z^{eff} \sim d_z - \sigma_{H_2Ow}$  in the narrower pore is very close to  $\frac{1}{2}$  of the wider one ( $\sigma_{H_2Ow}$  is the water-wall contact distance,  $\sim 0.345$  nm in our model system). The models for the solution are SPC/E<sup>30</sup> water and Joung-Cheatham<sup>31</sup> ion model adapted to selected water potential. These force fields are chosen because they capture reasonably well the properties of bulk solutions and are a good option when polarizable models are too computationally expensive. The confined solution is open to exchange with bulk environment of variable input pressures  $P_{bulk}$  and temperature  $T=298.15$  K.

Confinement simulations in this study use only perfectly smooth, parallel-plate walls based on the integrated 9-3 Lennard Jones (LJ) potential.<sup>17, 32-33</sup> The uniform-wall representation is advantageous as it secures rigorous validity<sup>34</sup> of the area-scaling approach<sup>35-36</sup> in interfacial tension calculations. The smooth wall/water interaction is described by the following equation

$$U_i(r) = A_i \left( \frac{\sigma_{iw}}{|z_i - z_w|} \right)^9 - B_i \left( \frac{\sigma_{iw}}{|z_i - z_w|} \right)^3 \quad (1)$$

where,  $A_i = 4/45\pi\rho_w\sigma_{iw}^3\varepsilon_{iw}$ ,  $B_i = 15A_i/2$ ,  $\rho_w$  is uniform density of the interacting sites in the wall,  $\sigma_{iw}$  and  $\varepsilon_{iw}$  are the mixed LJ parameters of originally chosen to describe water-wall interaction

using the Lorentz-Berthelot mixing rules, and  $z_i$  is the  $z$ -position of molecule  $i$  and  $z_w = d_z$  or  $z_w = 0$ .  $d_z$  is the distance between the walls.<sup>17, 19</sup> Values were originally chosen to fit a hydrocarbon wall (water contact angle of a cylindrical nanodrop<sup>37</sup>  $\theta = 127 \pm 3^\circ$ ) and are  $\rho_w = 0.333 \text{ \AA}^{-3}$ ,  $\varepsilon_w = 0.6483 \text{ kJ mol}^{-1}$ , and  $\sigma_w = 3.742 \text{ \AA}$ . Since eq 1 describes interactions with semi-infinite walls, periodic boundary conditions are not necessary in describing wall/solution interactions.

Laterally periodic boundary conditions are applied to mimic a nanopore of infinite  $(x,y)$  dimensions. Long range electrostatic interactions are calculated using Ewald summation with a slab-correction term developed by Yeh and Berkowitz.<sup>38</sup> The real-space cutoff value used is  $R_c = 9.8 \text{ \AA}$  with a screening parameter  $\alpha = \pi/R_c$  and  $15 \times 15 \times 19$  vectors in reciprocal space  $(k_x, k_y, k_z)$  and an identical cutoff is applied to the smoothly truncated water/water, water/ion, and ion/ion LJ interactions without tail correction. In an earlier work, we tested a suitable correction scheme applicable to the pore geometry<sup>19</sup>, however, its use becomes questionable in the nonperiodic situations encountered during the infiltration or expulsion stages, which represent the critical steps in our simulations. To preserve correct contents of water and ions in the open ensemble simulation, our input chemical potentials include a shift corresponding to the lack of respective tail contributions.<sup>14</sup>

**B. Simulation techniques.** Simulations are conducted primarily using the recently developed expanded ensemble Grand Canonical Monte Carlo (EEGCMC), as described in detail in previous works.<sup>39-42</sup> Unlike neat water,<sup>43-47</sup> open system simulations of electrolyte solutions have been notoriously challenging because of astronomically low acceptances of ion exchanges associated with extreme free energies<sup>31, 48-52</sup> of hydration. The above, well-tested open ensemble method relies on iteratively adding/removing molecules from the system using a biasing potential<sup>53</sup> to increase the likelihood of acceptance. In this work, water exchanges are split into 5 fractional steps

while ions have 15 fractional steps and are added in pairs to maintain the condition of neutrality in the system. Relevant thermodynamic averages are only calculated for configurations in which there are no fractional molecules. The EEGCMC method is used to simulate pore concentrations corresponding to bulk molalities of aqueous NaCl 5.70 mol kg<sup>-1</sup> (just below the solubility limit at ambient conditions), 4.28 mol kg<sup>-1</sup>, 3.02 mol kg<sup>-1</sup>, and 0 (neat water). Values for bulk concentrations are chosen based on the availability of experimental data for solution densities and associated chemical potentials which allows us to conduct high pressure simulations.<sup>16</sup> Simulations with this method for neat water system are run for 1x10<sup>9</sup> Monte Carlo (MC) steps where a step is either translation/rotation of a full molecule (69% chance), translation/rotation of a fractional molecule(20% chance), an iteration in fractional state (10% chance), or a simultaneous translation of the walls (1%)<sup>17</sup>. The same probabilities are used for systems with salt solutions, but the duration of the run is increased to 5x10<sup>9</sup>-1x10<sup>10</sup> depending on the pore size. The approximate duration for a single aqueous electrolyte run is between 3-6 processor months.

Presuming an equilibrium between the bulk and confined phases, the chemical potentials of confined species equal those in the bulk, which allows us to determine the pore compositions based on the input chemical potentials,  $\mu_i$ , for the two components. Ignoring scarce deviations from electroneutrality<sup>54</sup>, we consider only transfers of water and neutral ion pairs. Most reported simulations of open electrolyte systems have been performed with  $P = 1$  bar; however, we are interested in cases where pressure can vary from the ambient value to several kbar. Values for chemical potentials of aqueous NaCl across a range of pressures are not readily available in the literature but have now been calculated for 4 concentrations including neat water. The chemical potential, from previous work<sup>41</sup>, for water and NaCl,  $\mu_{\text{H}_2\text{O}}^*$  and  $\mu_{\text{NaCl}}^\dagger$ , at  $T = 298.15$  K and  $P_{\text{bulk}} = 1$  bar is -240.301 kJ mol<sup>-1</sup> and -391.278 kJ mol<sup>-1</sup>, respectively, with ideal gas contributions,  $\mu_{\text{H}_2\text{O}}^0$

and  $\mu_{\text{NaCl}}^0$ , which can be found in the NIST-JANAF thermochemical tables<sup>55</sup>, of  $-228.582 \text{ kJ mol}^{-1}$  and  $334.15 \text{ kJ mol}^{-1}$ , respectively. Chemical potentials at ambient pressure vary with salt concentration as reported in our previous work.<sup>19</sup> At elevated pressures, they are estimated from the ambient values adjusted using experimental partial molar volume data from ref. <sup>16</sup> as detailed in the following section.

### III. RESULTS AND DISCUSSION

**A. Chemical Potentials at High Pressure.** In a GCMC simulation, changes to the chemical potential of each species determine the equilibrium composition. By utilizing reported partial molar volumes as functions of pressure for a set of molalities<sup>16</sup>  $m$  we calculate chemical potentials of water and salt at different pressures  $P_{\text{bulk}}$  according to the relation

$$\mu_i(T, P_2, m) = \mu_i(T, P_1, m) + \int_{P_1}^{P_2} \bar{V}_i(T, P, m) dP \quad (2)$$

where, temperature,  $T$ , is constant at 298.15 K,  $\mu_i(T, P_2, m)$  is the chemical potential at given pressure,  $P_2$ ,  $\mu_i(T, P_1, m)$  is the chemical potential at the reference pressure  $P_1 = 1 \text{ bar}$  and  $\bar{V}_i$  is the partial molar volume of species  $i$  at given  $(T, P, m)$  state. The integral term  $\bar{V}_i dP$  pertains to the molar volume in the liquid phase and the externally applied pressure,  $P_{\text{bulk}}$ . In principle, equivalent results for chemical potentials should follow from integrating partial molar volumes in the gaseous phase over the corresponding range of *vapor pressures*,  $P_v$ , however, this route is not practically applicable to the salt component. Figure 1 presents chemical potentials from eq 2 for neat water and the 4 bulk molalities of NaCl used in this study:  $5.70 \text{ mol kg}^{-1}$ ,  $4.28 \text{ mol kg}^{-1}$ ,  $3.02 \text{ mol kg}^{-1}$ ,  $0$  (neat water). The applicability of chemical potentials from Figure 1 to our *model* system is

validated by the good agreement between computed bulk compositions at high pressures with the input molalities<sup>16</sup> from the experiment.

**B. Intrusion/Extrusion.** The main portion of this project is devoted to studies of the intrusion and extrusion of aqueous electrolytes into/from hydrophobic pores of preselected sizes  $d_z = 1.0$  nm and 1.64 nm to determine compositions and relevant thermodynamic properties in equilibrated systems. The narrower pores are considered because of their compelling energy storage properties<sup>13</sup>, and the wider pore size is chosen just above the threshold width supporting a metastable liquid phase in decompressed neat water<sup>17, 19, 27</sup>, so there would be an obvious difference in intrusion/extrusion properties.

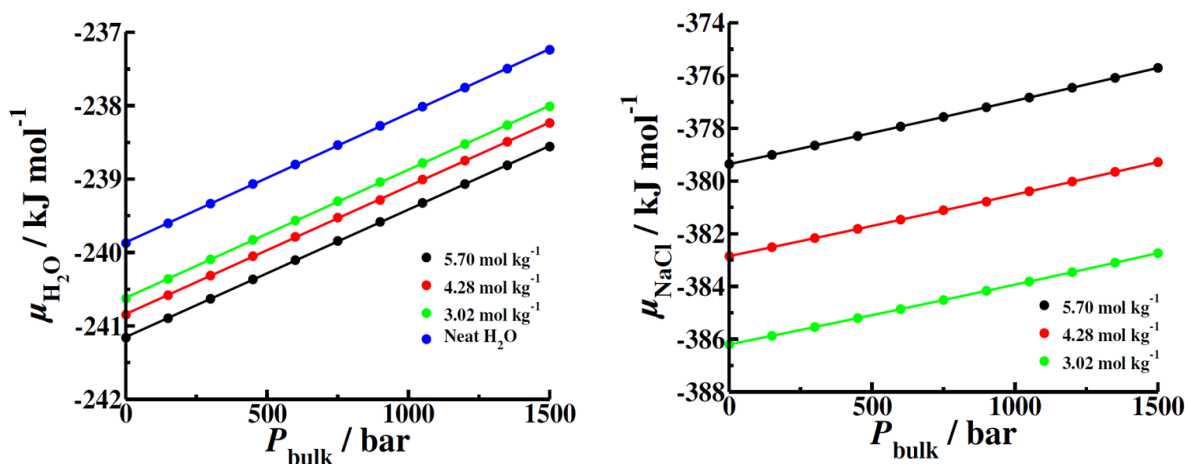


**Figure 1.** Input chemical potential values for water, left, and NaCl, right. Each value corresponds to a user determined pressure. Three concentrations used in these simulations are: 5.70 mol kg<sup>-1</sup> (black), 4.28 mol kg<sup>-1</sup> (red), 3.02 mol kg<sup>-1</sup> (green). Blue points correspond to neat H<sub>2</sub>O.

To study the extrusion branch, simulations pores were first filled by increasing the pressure to 3000 bar. Subsequently, the system was allowed to relax to the desired input pressure. When these simulations resulted in a stable (or metastable) liquid-filled pore, the final configuration was modified to generate the initial configuration in the intrusion simulations. For this purpose, the volume of the box was doubled by extending the box length along one of the two lateral dimensions with the pore diameter  $d_z$  being unchanged. The newly created volume contained no solvent

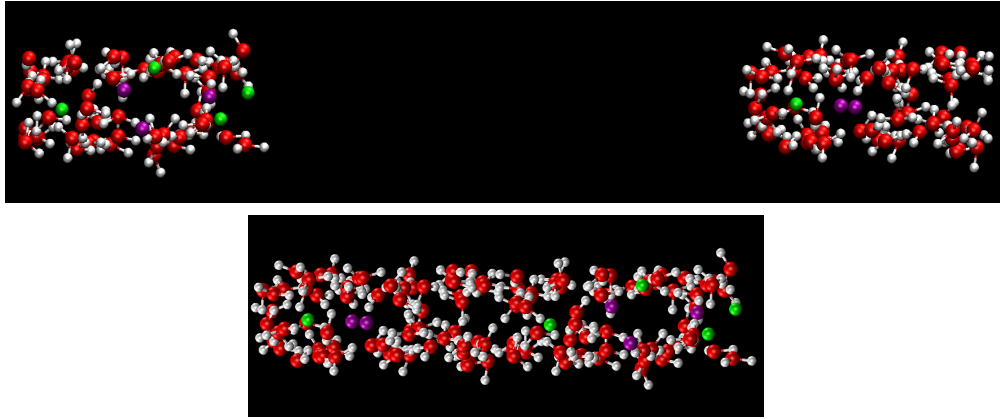


**Figure 2:** Snapshots of the elementary Monte Carlo boxes used in the simulation of confined NaCl solution inside the 1 nm pore during pressure relaxation (bottom), and the half-empty double size box generated by expanding the original (bottom) box to initiate an attempted infiltration run (see main text). The dark background spans the solvent-accessible width between soft pore walls placed at  $z_w=0$  and  $d_z=1$  nm (eq 1).

molecules or salt ions to resemble the solution infiltration process in real systems (see Figure 2). The procedure removes the free-energy barrier that would have been required for the liquid nucleation in a completely empty pore, a process that is not representative of experiments where the liquid phase resides at the opening. Conversely, the barrier to vapor nucleation cannot be avoided in the reverse process of solution *expulsion* upon lowering  $P_{\text{bulk}}$ , explaining the pronounced hysteresis of the cycle. Resulting intrusion/extrusion plots for the narrow pore are shown in Figure 3 and the results for the wider pore are shown in Figure 4. Due to the difficult nature of adding and removing an ion pair in solution, slow convergence when transitioning from an evacuated to permeated state, and comparatively low numbers of salt molecules, average numbers of ion pairs are associated with larger uncertainty than with water. The statistical error in the pore composition in the intrusion branch could in principle be reduced with longer simulations, but this becomes too costly and the added accuracy would not alter the central result, *i.e.* the intrusion pressure for given system. Since each of these calculations begins with a partially empty pore, impractical computation

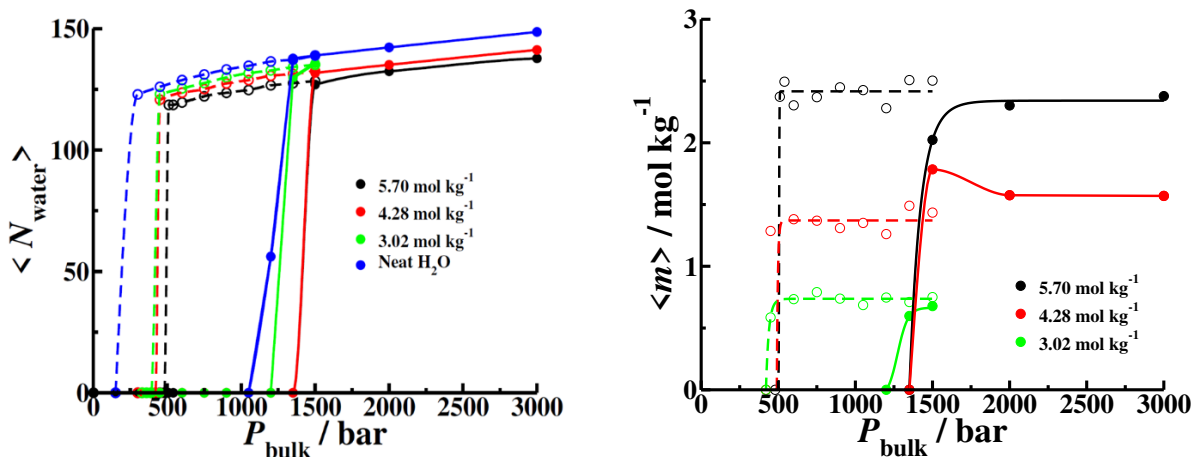


**Figure 3.** Intrusion (solid lines) and extrusion (dashed lines) of water, left, and NaCl, right, in a 1.0 nm pore for 3 bulk concentrations: 5.70 mol kg<sup>-1</sup> (black), 4.28 mol kg<sup>-1</sup> (red), 3.02 mol kg<sup>-1</sup> (green) and neat water (blue). NaCl is reported in terms of pore molality, while waters are counted by their total number. A surprising outcome is a *disproportionate* exclusion of the salt at low bulk concentration. Lines are to guide the eyes only. Error bars for water uptake: symbol size, molalities in extrusion branch:  $\pm 5\%$ . Intrusion molalities have not reached equilibrium.

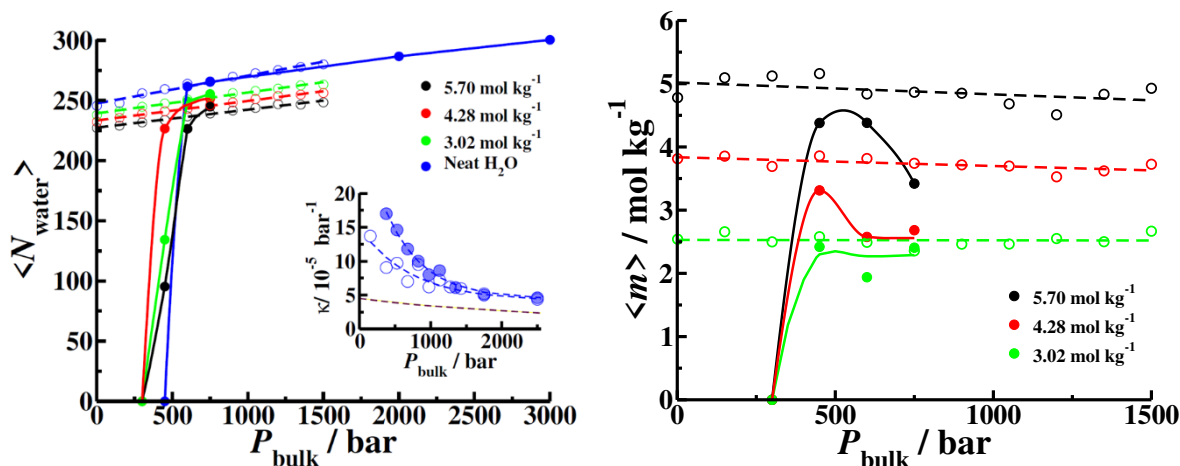


**Figure 4.** Intrusion (solid lines) and extrusion (dashed lines) of water, left, and NaCl, right, in a 1.64 nm pore for 3 bulk concentrations: 5.70 mol kg<sup>-1</sup> (black), 4.28 mol kg<sup>-1</sup> (red), 3.02 mol kg<sup>-1</sup> (green) and neat water (blue). NaCl is reported by pore concentration, while water is counted by its total number. There is a *proportionate* increase of pore concentration with increasing bulk electrolyte concentration. Lines are to guide the eyes only. Longer runs would be necessary to improve the accuracy in intrusion simulations containing salt solutions. Inset (left): Compressibility for water in a 1 nm pore, blue shaded circles, in a 1.64 nm pore, blue open circles, and in the bulk, dashed magenta line. The magenta dashed line shows bulk water compressibilities from experiment<sup>16</sup>. Error bars for water uptake: symbol size, molalities in extrusion branch:  $\pm 5\%$ . Intrusion molalities have not reached equilibrium. Compressibilities: up to  $\pm 8\%$ .

times (9-12 processor months for the wider, 1.64 nm pore) would be needed to secure converged

equilibration of pore composition. The main information provided by the intrusion curves is hence the estimation of the intrusion pressures. The intrusion process in the simulated system is much more abrupt than seen in experiments, where a degree of pore size polydispersity cannot be avoided. Pore concentrations after the intrusion, on the other hand, show considerable fluctuations and generally deviate from the stable values determined in the decompression branch of each cycle. Interestingly, the compositions of incompletely equilibrated states along the intrusion branches suggest the pore salt molality can pass through a maximum in the early stages of the infiltration.

The intrusion pressures  $P_{in}$  required to force water and NaCl into a hydrophobic pore are within the range observed in experiments.<sup>9, 12, 22, 56</sup> Consistent with the macroscopic prediction<sup>17</sup>  $P_{in} \approx \frac{2\gamma\cos\theta}{d_z^{eff}}$ ,  $P_{in}$  increases with decreasing pore width  $d_z^{eff}$  but the change is steeper than expected with given difference between the two widths we use. This is a clear indication of a simultaneous increase of the effective hydrophobicity of the walls as the liquid is forcefully compressed against them. We will return to this point in coming paragraphs where we analyze the pressure effect on wetting energetics. In doing so, we will only be assessing pure confinement effects between idealized unchanging walls without considering specific contributions indicated in zeolite experiments with changing extents of hydrophilic defects<sup>9</sup>, and frequent deformations after the first intrusion step.<sup>8</sup> Our observations are consistent with previous findings that the 1.64 nm pores do not empty upon releasing the pressure while the 1.0 nm pores empty near 500 bar for salt solutions and 150 bar for neat water.

The inset in Figure 4 presents the results for compressibility of confined water,  $\kappa = \left(\frac{\partial \ln N}{\partial P_{bulk}}\right)_{V,T}$  at elevated pressures.  $N$  is the number of liquid molecules in the confinement. Results in Figure 4 represent finite difference estimates for the slope of calculated  $\ln N$  vs.  $P_{bulk}$ . In the narrower pore, where the composition (molality) shows no detectable dependence on  $P_{bulk}$  (Figure

3), the same relation provides an estimate of the compressibility of the solution. In analogy with pure water<sup>17-18, 57-59</sup>, solution compressibility is increased inside a hydrophobic confinement, although less than for pure solvent, the compressibility of 5.7 mol kg<sup>-1</sup> solution at  $d_z=1$  nm and  $P_{\text{bulk}}$  near  $5 \cdot 10^2$  bar being close to  $\frac{1}{2}$  of that for confined water. Increased pressure leads to lower confinement compressibilities<sup>17</sup>, an effect akin to increasing the hydrophilicity of the walls. The higher compressibility in the confinement is primarily due to the pressure-induced buildup of the first hydration layer (see Section III.A). Because the interfacial region represents a bigger fraction of volume in the narrower pore, the compressibility rise is more pronounced there but the results for two pore sizes gradually converge with increasing pressure. Compression reduces the deviation from the bulk compressibility<sup>16</sup>; however, for pressures considered here, the confinement values never descend to those found in the bulk. The liquid uptake therefore continues to rise with compression even at extreme  $P_{\text{bulk}} \sim 3\text{kbar}$ . Salt ions accumulate in the pores in parallel with that of water, maintaining nearly constant equilibrium molalities in the pores.

The qualitative differences under released pressure separate the energy storage mechanisms of the 2 pore sizes with the larger pore displaying a bumper behavior, for all concentrations, and the smaller pore being the shock-absorber type, which allows for partial regeneration of input mechanical energy. At intermediate pressures, the liquid remains trapped in a metastable state<sup>17-18, 60</sup> because of considerable kinetic barrier  $\Delta\Omega^*$  to evaporation.<sup>24-29</sup> In the narrow pore, the barrier is eventually overcome at sufficiently low pressures. However,  $\Delta\Omega^*$  increases dramatically with pore widths ( $\Delta\Omega^* \propto d_z^2$ )<sup>28</sup> preventing expulsion from the wider pores across the entire pressure range and pragmatically relevant times. It then becomes desirable to see what thermodynamic and/or configurational changes drive these two behaviors.

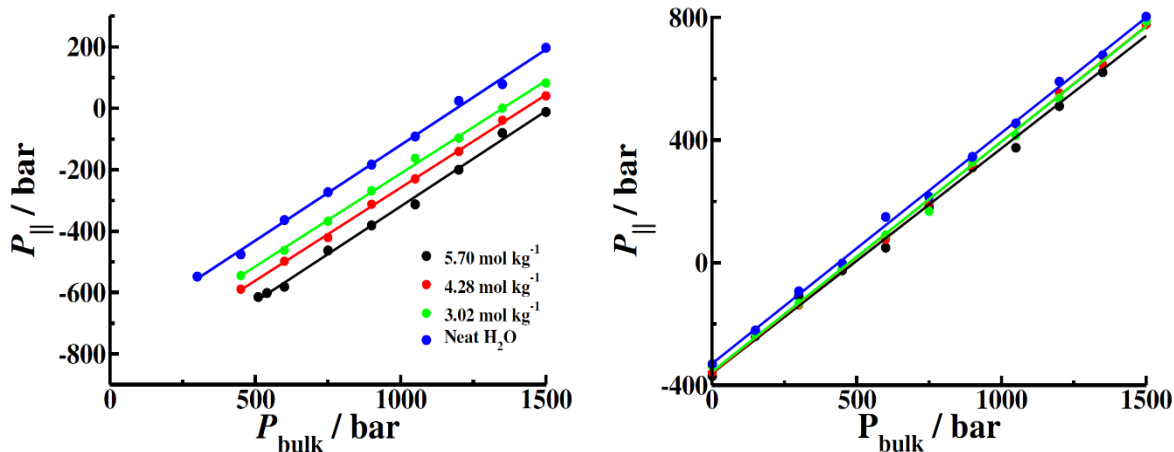


**Figure 5.** Dependence of the parallel pressure component,  $P_{\parallel}$  on the bulk pressure in 1.0 nm (left) and 1.64 nm pore (right). Error bars have been estimated at  $\pm 10$  bar in the narrower pore and  $\pm 20$  bar in the wider one.

**C. Thermodynamics.** While pressure tensors inside the pore are strongly anisotropic, all tensor components show a similar increase with the pressure applied in bulk solution. Figure 5 illustrates an almost linear relationship between the applied pressure,  $P_{\text{bulk}}$ , and the parallel pressure components ( $P_{\parallel}=P_{xx}=P_{yy}$ , averaged over the total width of the pore). Following previous work,  $P_{\parallel}$  is calculated as the (numerical) derivative of the system's free energy with respect to liquid expansion along lateral coordinates  $x$  or  $y$  at fixed  $d_z$ .<sup>36</sup> Similar data for the normal pressure,  $P_N$ , are shown in Fig. S1 in the Supplementary Information. At both pore sizes, the individual components increase by approximately the same amount as the input bulk value over the entire range of  $P_{\text{bulk}}$ . As shown in the preceding work<sup>19</sup>, the normal component of the pressure tensor in the confinement (Fig. S1) exceeds the bulk value and the difference depends on the salt concentration. The reduction of the components parallel to the plates,  $P_{\parallel}$ , reflects the strongly hydrophobic character of our model walls.

Despite the similarities between the two pore sizes, a more careful inspection of Figure 5 reveals smaller slopes in the narrower pore. Since the composition of the pore changes only slightly with pressure, we attribute the slope change primarily to the differences in the strength of

molecular interactions. Figure 6 shows the net energies, normalized by the number of molecules, are generally bigger in the wider pores characterized by a higher molecular coordination. The negative slopes of net energy vs.  $P_{\text{bulk}}$ , observed in the narrower pores, are consistent with higher compressibility and the resulting pressure-induced increase in the population of interacting neighbor molecules in these systems. Average potential energies of the pores of both sizes rapidly decrease with increasing ion concentration and the reduction is bigger in the wider pore characterized by much stronger uptake of the ions. The noise in the energy curves (Figures 6-7) is due to the very slow convergence of ion content in the pores; this is also suggested by the apparent correlations among adjacent points that can be traced down to common ancestor configurations.

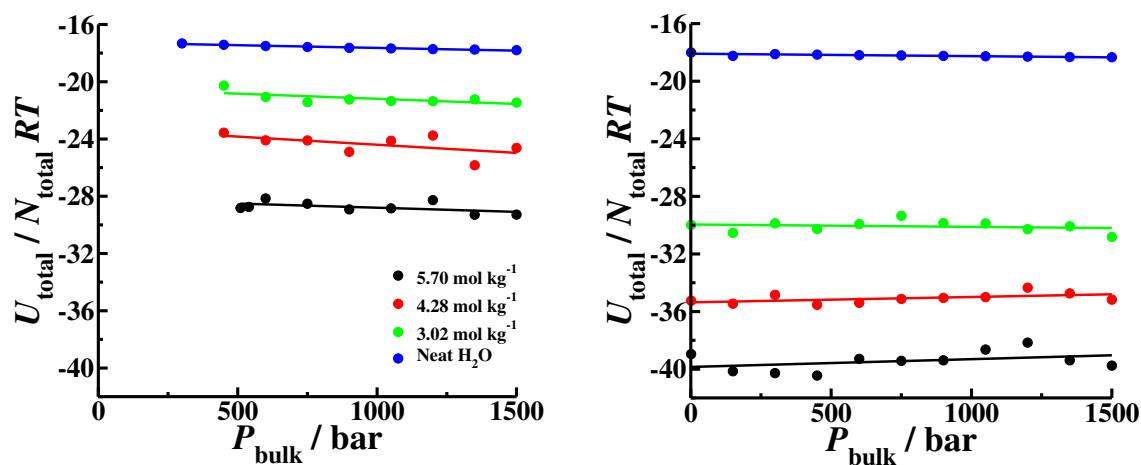


**Figure 6.** Total potential energy,  $U_{\text{total}}$ , for pores of size 1.0 nm (left) and 1.64 nm (right). The energy calculation includes the interaction with the walls and is normalized by the total number of particles (ions and water molecules) times thermal energy ( $RT$ ). The data for the narrower pore are limited to pressures that can sustain a stable or metastable liquid phase in the pore. Error bars of reduced energies in neat water are below symbol size while they are between  $\pm 0.5$  and 1 in solutions.

Figure 3 and Figure 4 show that the pore concentrations in the larger pore are approximately 85% of the bulk concentration with virtually no variation. On the other hand, the 1.0 nm pore has 23%, 32% and 42% of the following input bulk concentrations: 3.02 mol kg<sup>-1</sup>,

4.28 mol kg<sup>-1</sup>, and 5.70 mol kg<sup>-1</sup>, respectively (Figure 8). This implies a higher *relative* desalination when the concentration is lower, and the size of the pore is small enough. The results in Figure 8 indicate 1.0 nm porosity to enable a rather effective filtering capacity in reverse osmosis desalination. This capacity is shown to improve at reduced concentrations with extrapolation to sea water concentration suggesting almost complete separation.

The role the ions play in nanopore absorption can be partially explained by monitoring distinct contributions to the net intermolecular interaction inside the pore (Figure 7). Lennard-Jones energies represent a minor term in ion-ion interactions and the normalized values (energies per ion) show a very weak dependence on the salt concentration. This interaction alone does not tell much on its own, but combined with the structure within the pore, (next Section), we observe an increased structure for water with ions residing solely in the center of the pore physically separated from each other by hydrating waters. Electrostatic interactions for specified component pairs show moderate changes with pressure, however, a clear trend is hard to separate from the noise associated with slow equilibration and convergence of ion content.

The decrease in ion charge interactions seen with smaller concentrations is due to the disproportionately smaller pore concentrations. Inclusion of ions reduces water-water electrostatic interactions favoring instead water-ion interactions.

A key property quantifying the surface wettability is the interfacial free energy,  $\sigma$ , (the derivative of the grand potential  $\Omega$  with respect to the wetted area of pore walls) which we determine according to the relation<sup>19, 36, 61</sup>

$$\sigma = -\frac{1}{2}d_z P_{\parallel} \quad (3)$$

where  $d_z$  is the distance between the walls, and  $P_{\parallel}$  corresponds to the pressure component parallel

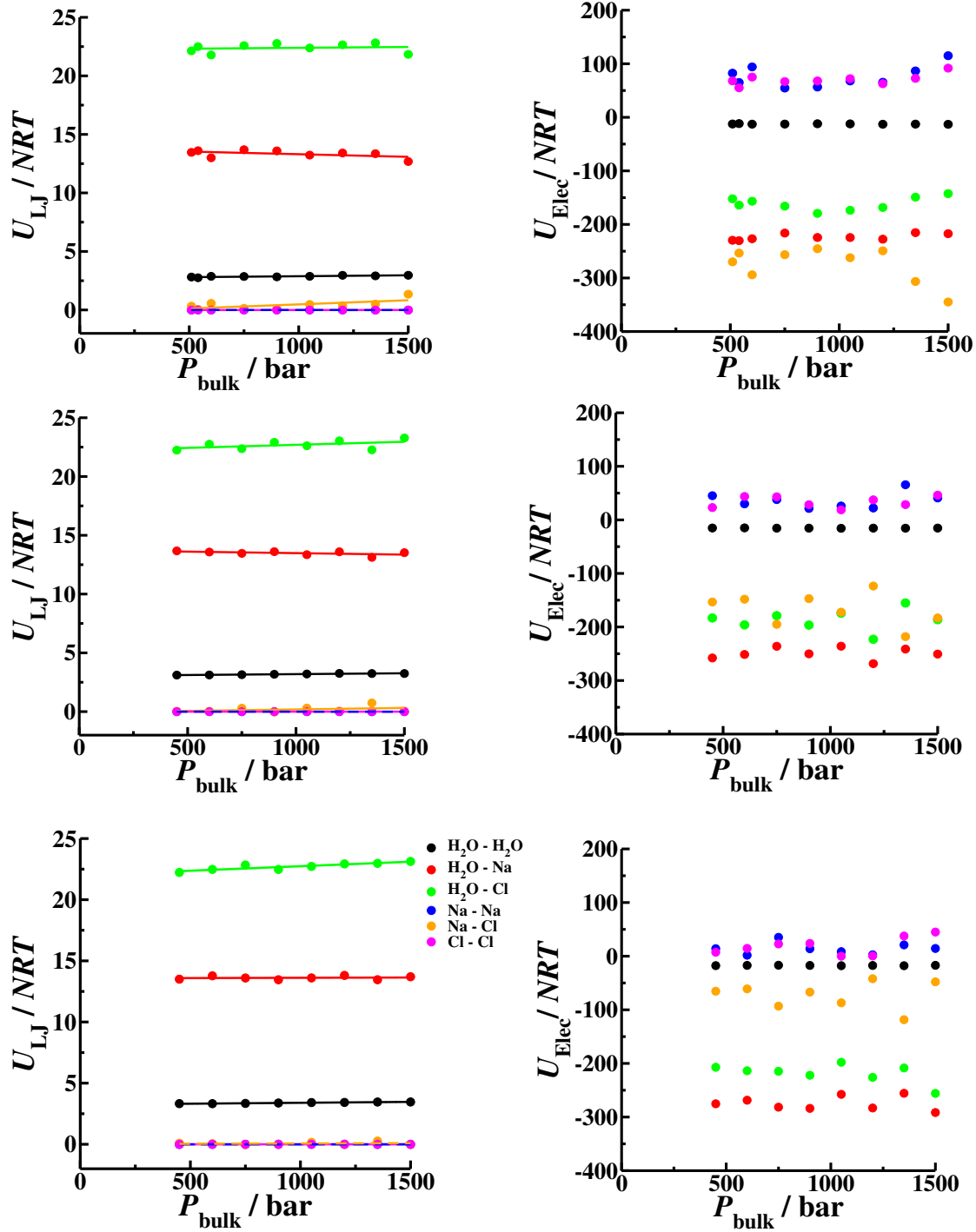


**Figure 7.** Lennard Jones (left) and electrostatic (right) pairwise interactions for H<sub>2</sub>O and NaCl in a 1.0 nm pore. Values are normalized by dividing by  $N$  times thermal energy  $RT$ . For water-water interactions,  $N$  represents the number of water molecules; otherwise,  $N$  is the number of ion pairs. Input bulk molalities are: top 5.70 mol kg<sup>-1</sup>, middle 4.28 mol kg<sup>-1</sup>, bottom 3.02 mol kg<sup>-1</sup>. The fluctuations in the energies are associated with slow equilibration of pore compositions used in subsequent calculations of distinct energy contributions in  $NVT$  simulations. In cases where lines overlap various dashed styles have been used for clarity. Statistical uncertainties of Lennard Jones energies and electrostatic energies among water molecules are close to symbol size or smaller. Error bars for electrostatic terms carry error bars of  $\pm 20$  for Na<sup>+</sup>-Na<sup>+</sup> and Cl<sup>-</sup>-Cl<sup>-</sup> pairs,  $\pm 40$  for Na<sup>+</sup>-Cl<sup>-</sup> pairs, and  $\pm 35$  for both ion-water component pairs.

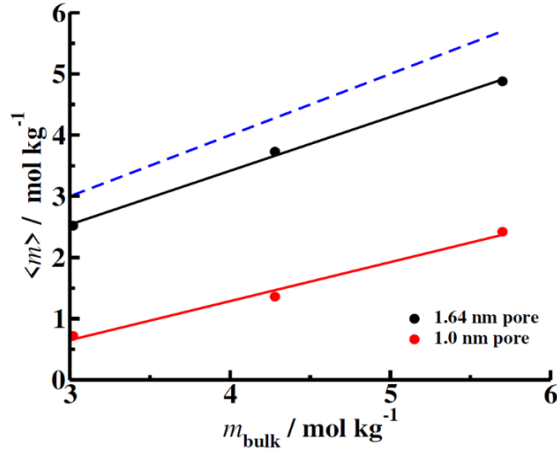


**Figure 8.** Average nanopore molality,  $m$ , shown against the bulk concentration,  $m_{\text{bulk}}$ , at the lowest pressure supporting pore permeation. The blue dashed line represents a situation where the pore concentration is equal to the bulk concentration. The 1.0 nm pore (red), shows a much larger salt depletion than observed in the 1.64 nm pore (black). Furthermore, the *relative* desalination is more pronounced when the concentration is lower, but only in the narrower pore. At both pore widths, molality in the confinement is essentially insensitive to  $P_{\text{bulk}}$  (Figures 3-4).

to the plates (The reader is referred to ref.<sup>36</sup> for a full discussion of eq 3 and details of  $P_{\parallel}$  calculation). The more negative this value is the greater the tendency to wet becomes (Figure 9). We, therefore, can approximately predict at what pressure intrusion will occur by pinpointing when  $\sigma$  switch signs and we find a direct agreement with Figure 3 and Figure 4. In the wider pore, the  $\sigma$  values appear relatively insensitive to the concentration consistent with the weak effect of ions on the tendency for the pore to be filled. A bigger separation of  $\sigma$  values for different concentrations in the 1.0 nm pore is associated with a stronger influence of the salt on intrusion pressures (Figure 3).

The trends discussed so far relate pore properties to the input (experimental) bulk pressures,  $P_{\text{bulk}}$ . Replacing experimental pressures by the *model* bulk pressures devoid of the tail contribution (consistent with the calculation in the pore) would suggest a shift of  $P_{\text{bulk}}$  values equivalent to subtracting the (negative) tail correction  $\Delta P_{\text{tail}} = \sum \rho_i \Delta \mu_i^{\text{tail}} = O(-10^2)$  bar. ( $\rho_i$ -s denote number

densities of solution components  $i$ ). This is avoided through the use of adjusted chemical potentials (Section II.A). The consistency of pressures in the pore with the input  $P_{\text{bulk}}$  is corroborated by the good agreement between the intrusion pressures from direct observation (Figures 3-4) with those corresponding to vanishing values  $\sigma$  (Figure 5).

In Figure 10 we also present the ‘pure’ wetting free energy,  $\sigma'$ , estimated by excluding the area derivative of the work  $-P_{\text{bulk}}dV$  against external pressure  $P_{\text{bulk}}$  during liquid intrusion. Since the volume occupied by the liquid varies in proportion to wetted area,  $dV \approx \frac{1}{2} d_z^{eff} dA_w$ ,  $\sigma'$  can be obtained from the relation

$$\sigma' \approx \sigma + \frac{1}{2} d_z^{eff} P_{\text{bulk}} \quad (2)$$

Results for  $\sigma'$  in Figure 10 quantify the actual surface resistance to wetting, showing that the walls appear somewhat more hydrophobic with increasing pressure<sup>62-63</sup> and with the concentration of ions. The effect of salinity is considerably stronger in the narrower, 1.0 nm pore. A deficit in the concentration can be found in confinement, but especially for the narrow pore (Figure 8). The observed trends of wetting free energy can be explained in terms of the Gibbs adsorption isotherm

$$\sigma(m_{\text{bulk}}, P_{\text{bulk}}) = \sigma(0, P_{\text{bulk}}) - \sum_i \int_{\mu_i(0)}^{\mu_i(m_{\text{bulk}})} \Gamma(\mu_i, P_{\text{bulk}}) d\mu_i \quad (3)$$

which relates surface adsorption to the changes in interfacial tension.<sup>40, 64</sup> Above,  $\Gamma(\mu_i, P_{\text{bulk}})$  represents the surface excesses of species  $i$  with the specified chemical potential and bulk pressure. Large surface deficits of ions in the narrow pore, *i.e.* strongly negative  $\Gamma(\mu_i, P_{\text{bulk}})$  imply a significant increase of  $\sigma$  upon increasing the bulk salinity. Conversely, the moderate salt depletion in the wider pores result in only a weak dependence of  $\sigma$  on the bulk salt concentration.

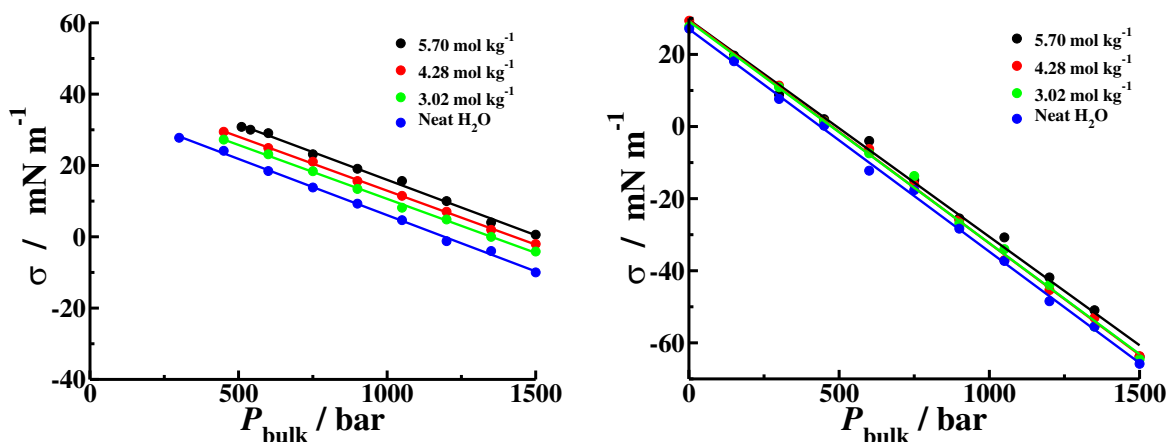


**Figure 9.** Wetting free energy versus the input bulk pressure is calculated from extrusion simulations and is displayed for a 1.0 nm pore (left) and 1.64 nm pore (right) for 3 concentrations: 5.70 mol kg<sup>-1</sup>, 4.28 mol kg<sup>-1</sup>, and 3.02 mol kg<sup>-1</sup>. The apparent tendency to wet increases with increasing pressure. Values for the 1.0 nm pore below 150 bar are omitted due to empty pores. Statistical error bars are estimated at up to  $\pm 1$  mN m<sup>-1</sup> in the narrower pores and  $\pm 2$  mN m<sup>-1</sup> in the wider ones.

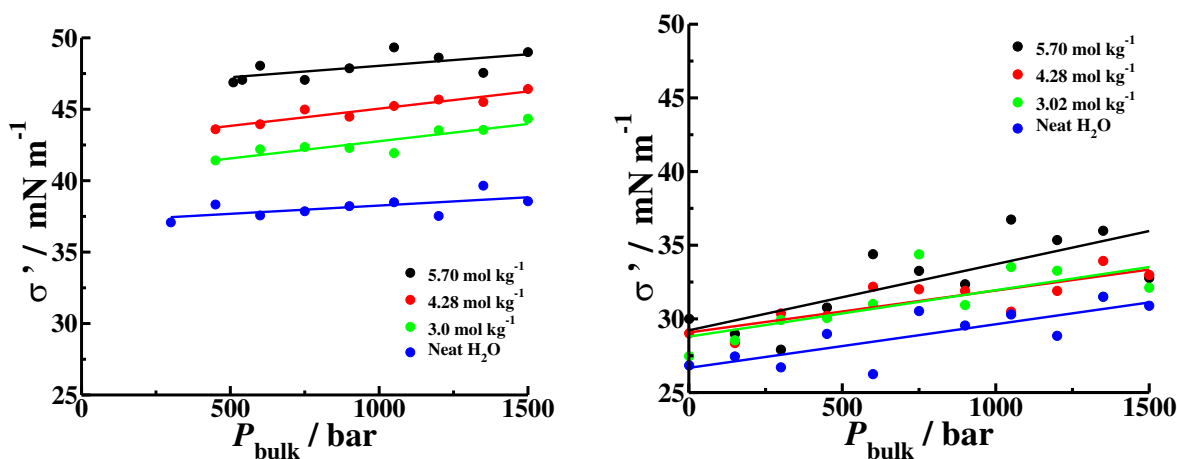


**Figure 10.** 'Pure' wetting free energy,  $\sigma'$ , is calculated from extrusion-branch simulations by excluding the contribution of external pressure,  $P_{\text{bulk}}$ , as the driving force for liquid infiltration (eq 4). Results for a 1.0 nm pore (left) and 1.64 nm pore (right), for neat water and 3 salt concentrations: 5.70 mol kg<sup>-1</sup>, 4.28 mol kg<sup>-1</sup>, and 3.02 mol kg<sup>-1</sup> show the walls appear more hydrophobic as solution is compressed into the pore. Values for the 1.0 nm pore below 260 bar are not available because of spontaneous expulsion of the liquid. Statistical uncertainties: up to  $\pm 1$  mN m<sup>-1</sup> in the narrower pores and  $\pm 2$  mN m<sup>-1</sup> in the wider ones.

**D. Structure.** To further elucidate the effects of compression within a nanopore we explore the structural features of each configuration. Density profiles shown in Figure 11 help explain the increase of wall hydrophobicity accompanying the increased packing in the pore. Because of steric

restraints, the majority of water molecules in the narrower pore populate distinct hydration layers next to the walls. This configuration results in a stronger deprivation of hydrogen bonds<sup>65</sup> than is the case in the wider pore, where the interfacial layers are separated by bulklike water, accounting for  $\sim 9 \text{ mN m}^{-1}$  difference in the pure wetting free energies for the two pore sizes observed even in the absence of salt. Because of the ions' tendency to preserve their hydration shells, they avoid direct contact with the walls. In the narrower pore, this trend confines the ions to a diffuse monolayer centered at the midplane of the pore. Nonetheless, cations and anions remain physically separated by water molecules and interact with each other only electrostatically (Figure 7). The additional space available in the wider pore allows the anions to spread out to their preferred location closer to the interface<sup>42</sup> while the density of the smaller and more strongly hydrated cations still peaks at the center of the pore, with secondary cation density peaks coinciding with the maxima of the anion distribution. The spatial separation of ions and concomitant oscillations in the charge densities due to the ions are matched by the opposite charge density contributions

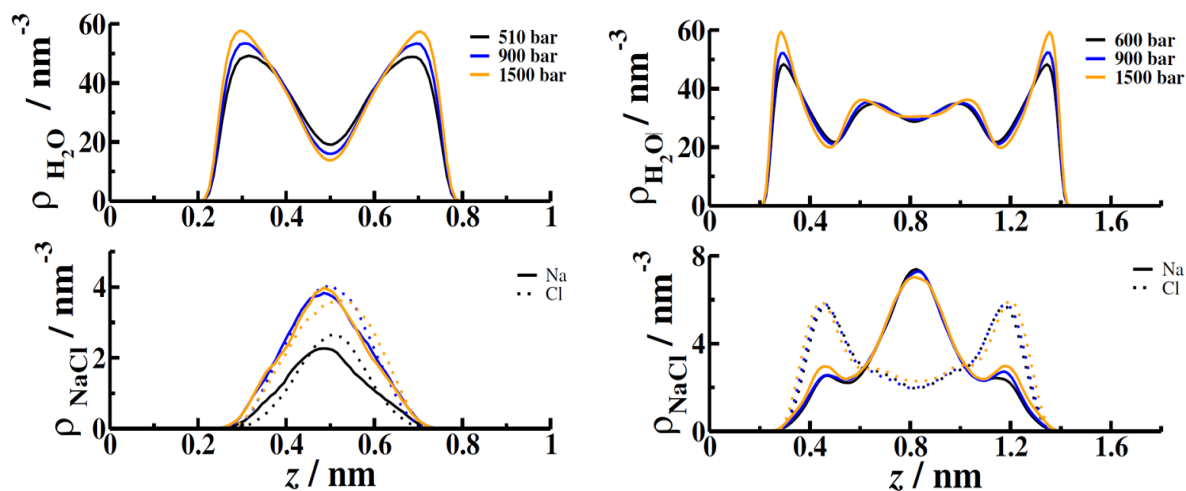


**Figure 11.** Number density profile of water, top, and NaCl ions, bottom, in confinement between a 1.0 nm pore, left, and a 1.64 nm pore, right. The location on the x-axis of one wall is always placed on 0. Of ions,  $\text{Na}^+$  is shown by solid lines and  $\text{Cl}^-$  has dotted lines, while the color coding matches for pressure inputs matches that for waters. These figures were created from extrusion simulations with bulk ion concentrations of  $5.70 \text{ mol kg}^{-1}$ .

from the partially charged atoms of water. We illustrate charge distributions in Figure 12. In the 1.0 nm pore, the charges from the ions almost completely cancel each other out, while water charge distributions reflect an enhanced structure imposed by the more restrictive confinement. In the wider pore, the orientational polarization of water is facilitated further by matching the charge layering due to the ions. Our earlier work<sup>19, 40</sup> showed this feature to facilitate the solution uptake and reduce the apparent hydrophobicity of the pore. Present results confirm the same mechanism continues to operate across the entire range of pressures, with density amplitudes gradually intensified with compression. Additional features, best manifested in the charge density profiles for the highest pressure (1500 bar) in Figure 12, are seen to develop in the highly compressed water in the wider pore. The increased structure gleaned from the high-pressure results in Figures 11 and 12 imply an entropy reduction that can rationalize the moderate increases in the pure wetting free energies,  $\sigma'$  (Figure 10) with increasing  $P_{\text{bulk}}$  even when the opposite trend is suggested from the decreasing energies observed in the narrower pore (Figure 6).

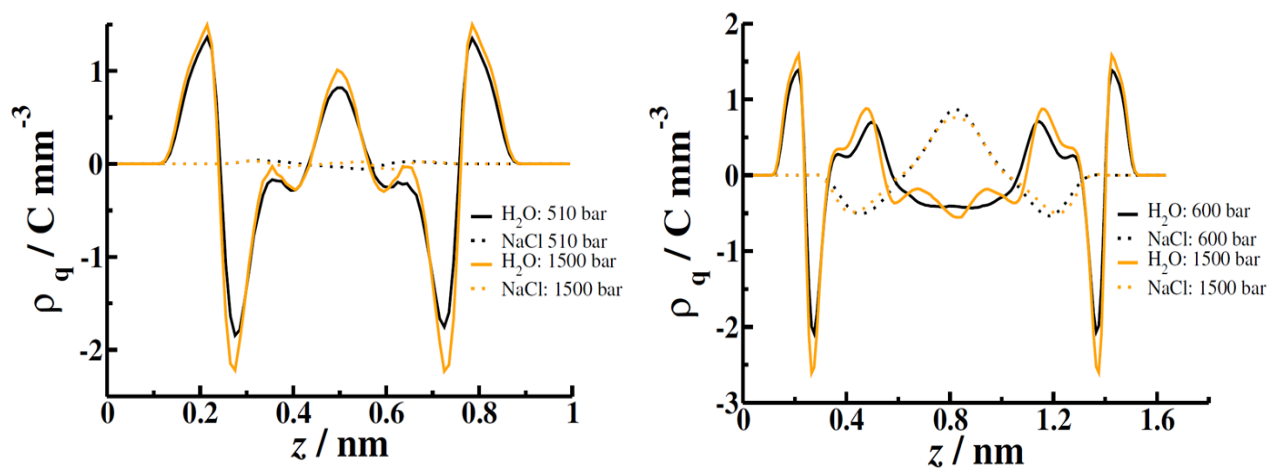


**Figure 12.** Charge density of molecules in confinement between a 1.0 nm pore, left, and a 1.64 nm pore, right. The location on the x-axis of one wall is always placed on 0. These figures were created from extrusion simulations with bulk ion concentrations of  $5.70 \text{ mol kg}^{-1}$ . A clear distinction in the packing of water molecules is observed for higher pressures. This increase in structure implies a requirement for water to reorient in order to compensate for the increased number density.

## IV. CONCLUSIONS

Through open ensemble simulations, we gain an insight into the mechanisms of the uptake of water and aqueous NaCl solutions in a wetting-resistant nanoporous medium over a large range of external pressures. By using pressure-dependent chemical potentials, derived from volumetric experiments, we are able to study confined systems open to pressurized bulk solutions. Our confinement model places the solution between perfectly smooth, hydrocarbon-like plates with separations of 1.0 nm and 1.64 nm to monitor the intrusion/extrusion cycle of solutions.

We find reversibility in our simulations to be consistent with literature, namely the infiltration of the narrower pore is reversible while wetting of the larger pore is irreversible. Reversibility creates a pathway for partial energy recovery characteristic of a shock-absorber material. The prominent hysteresis can be alleviated when pure water is replaced by aqueous electrolytes; NaCl was considered because of available volumetric data. The reduction in hysteresis is attributed to the increase of the pore/solution interfacial tension with increasing salt concentration. Based on the comparison between the two pore sizes we considered, only a slight reduction of the nano-sized pore width should suffice to remove the hysteresis, leading to liquid spring behavior. Additionally, the narrow pore presents a strong desalination effect, which is even more prominent for lower bulk concentrations of NaCl. The increase of liquid compressibility in hydrophobic confinements, previously studied in neat water, is still observed but weakens with increasing salt molality. While compressibilities corresponding to the two pore sizes converge at extremely high pressures, they never descend to that of the bulk phase.

As one would expect, a more structured confined system is observed with increasing pressure which produces stronger steric restraints on solvating waters especially in the narrow

pore. This effect, along with the surface depletion of salt ions, accounts for the differences observed in pure wetting free energies which tell that walls appear more hydrophobic as solution is compressed into the pore. The effect of salinity can be potentially enhanced by changing the system in future work. Namely, a considerably higher intrusion pressure would be expected if the salt solution were changed to LiCl since its solubility is near three times higher than for NaCl. It would also be of interest to consider molecular nanopores with narrow windows through which solution can flow into a larger space. This process, amenable to Molecular Dynamics or diffusive Monte Carlo, would create a situation where a higher desalination effect could likely be observed, changing the mechanism and amount of possible energy storage.

## ASSOCIATED CONTENT

\* Supporting Information

The Supporting Information is available free of charge on the [ACS Publications website](#) at DOI:

## ACKNOWLEDGEMENTS

We thank the Office of Basic Energy Sciences, Chemical Sciences, Geosciences, and Biosciences Division of the U.S. Department of Energy (Grant No. DE-SC 0004406) for support at early stages, and acknowledge support from the National Science Foundation (Grant No. CHE-1800120) during the late stage of the project. SZ thanks for generous support from an Altria Graduate Research Fellowship. FM acknowledges financial support from the Czech Science Foundation (Project No. 19-05696S). We also thank for the supercomputer time from Extreme Science and Engineering Discovery Environment (XSEDE), supported by NSF Grant No. OCI-1053575, and the National Energy Research Scientific Computing Center (NERSC), supported by the Office of Science of the U.S. Department of Energy (No. DEAC02-05CH11231).

## REFERENCES

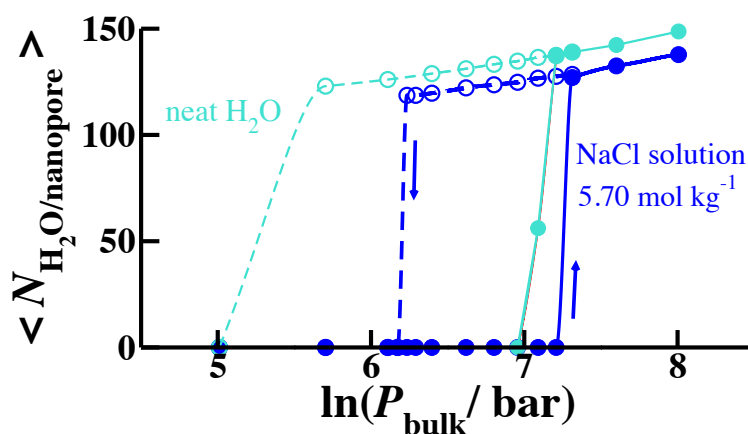
1. Grosu, Y.; Mierzwa, M.; Eroshenko, V. A.; Pawlus, S.; Chorazewski, M.; Nedelec, J. M.; Grolier, J. P. E. Mechanical, Thermal, and Electrical Energy Storage in a Single Working Body: Electrification and Thermal Effects Upon Pressure-Induced Water Intrusion Extrusion in Nanoporous Solids. *ACS Appl. Mater. Interfaces* **2017**, *9*, 7044-7049.
2. Grosu, Y.; Li, M.; Peng, Y. L.; Luo, D.; Li, D.; Faik, A.; Nedelec, J. M.; Grolier, J. P. A Highly Stable Nonhysteretic {Cu-2(Tebpz) Mof Plus Water} Molecular Spring. *ChemPhysChem* **2016**, *17*, 3359-3364.

3. Han, A. J.; Lu, W. Y.; Kim, T.; Chen, X.; Qiao, Y. Influence of Anions on Liquid Infiltration and Defiltration in a Zeolite Y. *Phys. Rev. E* **2008**, *78*, 4.
4. Eroshenko, V.; Regis, R. C.; Soulard, M.; Patarin, J. Energetics: A New Field of Applications for Hydrophobic Zeolites. *J. Am. Chem. Soc.* **2001**, *123*, 8129-8130.
5. Eroshenko, V.; Regis, R. C.; Soulard, M.; Patarin, J. The Heterogeneous Systems 'Water-Hydrophobic Zeolites': New Molecular Springs. *C. R. Phys.* **2002**, *3*, 111-119.
6. Soulard, M.; Patarin, J.; Eroshenko, V.; Regis, R., Molecular Spring or Bumper: A New Application for Hydrophobic Zeolitic Materials. In *Recent Advances in the Science and Technology of Zeolites and Related Materials, Pts. A-C*, 2004; Vol. 154, pp 1830-1837.
7. Xu, R.; Pang, W.; Yu, J.; Huo, Q.; Chen, J., *Chemistry of Zeolites and Related Porous Materials Synthesis and Structure*. Singapore ; Hoboken, N.J. : John Wiley & Sons Asia: Singapore ; Hoboken, N.J., 2007.
8. Ryzhikov, A.; Khay, I.; Nouali, H.; Daou, T. J.; Patarin, J. Drastic Change of the Intrusion-Extrusion Behavior of Electrolyte Solutions in Pure Silica (Star)Bea-Type Zeolite. *Phys. Chem. Chem. Phys.* **2014**, *16*, 17893-17899.
9. Ryzhikov, A.; Khay, I.; Nouali, H.; Daou, T. J.; Patarin, J. High Pressure Intrusion–Extrusion of Electrolyte Solutions in Aluminosilicate Fau and Bea-Type Zeolites. *Microporous and Mesoporous Mater.* **2016**, *221*, 1-7.
10. Ryzhikov, A.; Arletti, R.; Quartieri, S.; Vezzalini, G.; Confalonieri, G.; Isaac, C.; Paillaud, J.-L.; Nouali, H.; Daou, T. J. Structural Interpretation of the Energetic Performances of a Pure Silica Lta-Type Zeolite. *Phys. Chem. Chem. Phys.* **2020**, *22*, 5178-5187.
11. Han, A.; Qiao, Y. A Volume-Memory Liquid. *Appl. Phys. Lett.* **2007**, *91*.
12. Saada, M. A.; Rigolet, S.; Paillaud, J.; Bats, N.; Soulard, M.; Patarin, J. Investigation of the Energetic Performance of Pure Silica Itq-4 (Ifr) Zeolite under High Pressure Water Intrusion. *J. Phys. Chem. C* **2010**, *114*, 11650-11658.
13. Fraux, G.; Coudert, F. X.; Boutin, A.; Fuchs, A. H. Forced Intrusion of Water and Aqueous Solutions in Microporous Materials: From Fundamental Thermodynamics to Energy Storage Devices. *Chem. Soc. Rev.* **2017**, *46*, 7421-7437.
14. Frenkel, D.; Smit, B., *Understanding Molecular Simulation, from Algorithms to Applications*. Academic: San Diego, 2002.
15. Mao, S.; Duan, Z. H. The P,V,T,X Properties of Binary Aqueous Chloride Solutions up to T=573 K and 100 Mpa. *J. Chem. Thermodyn.* **2008**, *40*, 1046-1063.
16. Adams, L. H. Equilibrium in Binary Systems under Pressure. I. An Experimental and Thermodynamic Investigation of the System, NaCl-H<sub>2</sub>O, at 25o. *J. Am. Chem. Soc.* **1931**, *53*, 3769-3813.
17. Bratko, D.; Curtis, R. A.; Blanch, H. W.; Prausnitz, J. M. Interaction between Hydrophobic Surfaces with Metastable Intervening Liquid. *J. Chem. Phys.* **2001**, *115*, 3873-3877.
18. Giovambattista, N.; Rossky, P. J.; Debenedetti, P. G. Effect of Pressure on the Phase Behavior and Structure of Water Confined between Nanoscale Hydrophobic and Hydrophilic Plates. *Phys. Rev. E* **2006**, *73*, 041604.
19. Moucka, F.; Bratko, D.; Luzar, A. Electrolyte Pore/Solution Partitioning by Expanded Grand Canonical Ensemble Monte Carlo Simulation. *J. Chem. Phys.* **2015**, *142*, 124705.
20. Vanzo, D.; Bratko, D.; Luzar, A. Dynamic Control of Nanopore Wetting in Water and Saline Solutions under an Electric Field. *J. Phys. Chem. B* **2015**, *119*, 8890-8899.

21. Michelin-Jamois, M.; Picard, C.; Vigier, G.; Charlaix, E. Giant Osmotic Pressure in the Forced Wetting of Hydrophobic Nanopores. *Phys. Rev. Lett.* **2015**, *115*.
22. Ronchi, L.; Ryzhikov, A.; Nouali, H.; Daou, T. J.; Patarin, J. Energetic Performances of Fer-Type Zeolite in the Presence of Electrolyte Solutions under High Pressure. *Energy* **2017**, *130*, 29-37.
23. Lum, K.; Luzar, A. Pathway to Surface-Induced Phase Transition of a Confined Fluid. *Phys. Rev. E* **1997**, *56*, R6283-R6286.
24. Lum, K.; Chandler, D. Phase Diagram and Free Energies of Vapor Films and Tubes for a Confined Fluid. *Int. J. Thermophys.* **1998**, *19*, 845-855.
25. Leung, K.; Luzar, A. Dynamics of Capillary Evaporation. Ii. Free Energy Barriers. *J. Chem. Phys.* **2000**, *113*, 5845-5852.
26. Luzar, A.; Leung, K. Dynamics of Capillary Evaporation. I. Effect of Morphology of Hydrophobic Surfaces. *J. Chem. Phys.* **2000**, *113*, 5836-5844.
27. Leung, K.; Luzar, A.; Bratko, D. Dynamics of Capillary Drying in Water. *Phys. Rev. Lett.* **2003**, *90*, 065502.
28. Luzar, A. Activation Barrier Scaling for the Spontaneous Evaporation of Confined Water. *J. Phys. Chem. B* **2004**, *108*, 19859-19866.
29. Sharma, S.; Debenedetti, P. G. Free Energy Barriers to Evaporation of Water in Hydrophobic Confinement. *J. Phys. Chem. B* **2012**, *116*, 13282-13289.
30. Berendsen, H. J. C.; Grigera, J. R.; Straatsma, T. P. The Missing Term in Effective Pair Potentials. *J. Phys. Chem.* **1987**, *91*, 6269-6271.
31. Joung, I. S.; Cheatham, T. E. Determination of Alkali and Halide Monovalent Ion Parameters for Use in Explicitly Solvated Biomolecular Simulations. *J. Phys. Chem. B* **2008**, *112*, 9020-9041.
32. Lee, S. H.; Rossky, P. J. A Comparison of the Structure and Dynamics of Liquid Water at Hydrophobic and Hydrophilic Surfaces - a Molecular-Dynamics Simulation Study. *J. Chem. Phys.* **1994**, *100*, 3334-3345.
33. Shelley, J. C.; Patey, G. N. Boundary Condition Effects in Simulations of Water Confined between Planar Walls. *Mol. Phys.* **1996**, *88*, 385-398.
34. Mittal, J.; Hummer, G. Interfacial Thermodynamics of Confined Water near Molecularly Rough Surfaces. *Faraday Discuss.* **2010**, *146*, 341-352.
35. Bratko, D.; Daub, C. D.; Luzar, A. Water-Mediated Ordering of Nanoparticles in an Electric Field. *Faraday Discuss.* **2009**, *141*, 55-66.
36. Bratko, D.; Daub, C. D.; Leung, K.; Luzar, A. Effect of Field Direction on Electrowetting in a Nanopore. *J. Am. Chem. Soc.* **2007**, *129*, 2504-2510.
37. Vanzo, D.; Bratko, D.; Luzar, A. Wettability of Pristine and Alkyl-Functionalized Graphane. *J. Chem. Phys.* **2012**, *137*, 034707.
38. Yeh, I. C.; Berkowitz, M. L. Ewald Summation for Systems with Slab Geometry. *J. Chem. Phys.* **1999**, *111*, 3155-3162.
39. Moucka, F.; Lisal, M.; Skvor, J.; Jirsak, J.; Nezbeda, I.; Smith, W. R. Molecular Simulation of Aqueous Electrolyte Solubility. 2. Osmotic Ensemble Monte Carlo Methodology for Free Energy and Solubility Calculations and Application to NaCl. *J. Phys. Chem. B* **2011**, *115*, 7849-7861.
40. Moucka, F.; Bratko, D.; Luzar, A. Salt and Water Uptake in Nanoconfinement under Applied Electric Field: An Open Ensemble Monte Carlo Study. *J. Phys. Chem. C* **2015**, *119*, 20416-20425.

41. Moucka, F.; Nezbeda, I.; Smith, W. R. Chemical Potentials, Activity Coefficients, and Solubility in Aqueous NaCl Solutions: Prediction by Polarizable Force Fields. *J. Chem. Theory Comput.* **2015**, *11*, 1756-1764.
42. Moucka, F.; Zamfir, S.; Bratko, D.; Luzar, A. Molecular Polarizability in Open Ensemble Simulations of Aqueous Nanoconfinements under Electric Field. *J. Chem. Phys.* **2019**, *150*.
43. Desbiens, N.; Boutin, A.; Demachy, I. Water Condensation in Hydrophobic Silicalite-1 Zeolite: A Molecular Simulation Study. *J. Phys. Chem. B* **2005**, *109*, 24071-24076.
44. Zhang, H. D.; Snurr, R. Computational Study of Water Adsorption in the Hydrophobic Metal-Organic Framework Zif-8: Adsorption Mechanism and Acceleration of the Simulations. *J. Phys. Chem. C* **2017**, *121*, 24000-24010.
45. Tinti, A.; Giacomello, A.; Grosu, Y.; Casciola, C. M. Intrusion and Extrusion of Water in Hydrophobic Nanopores. *Proc. Natl. Acad. Sci. U. S. A.* **2017**, *114*, E10266-E10273.
46. Kolokathis, P. D.; Pantatosaki, E.; Papadopoulos, G. K. Modeling the Hydration-Induced Structural Transitions of the Sapo-34 Zeolite and Their Impact on the Water's Sorbed Phase Equilibrium and Dynamics. *J. Phys. Chem. C* **2020**, *124*, 11480-11489.
47. Zhou, T. C.; Bai, P.; Siepmann, J. I.; Clark, A. E. Deconstructing the Confinement Effect Upon the Organization and Dynamics of Water in Hydrophobic Nanoporous Materials: Lessons Learned from Zeolites. *J. Phys. Chem. C* **2017**, *121*, 22015-22024.
48. Hummer, G.; Pratt, L. R.; Garcia, A. E. Free Energy of Ionic Hydration. *J. Phys. Chem.* **1996**, *100*, 1206-1215.
49. Hummer, G.; Pratt, L. R.; Garcia, A. E. Molecular Theories and Simulation of Ions and Polar Molecules in Water. *J. Phys. Chem. A* **1998**, *102*, 7885-7895.
50. Hummer, G.; Pratt, L. R.; Garcia, A. E.; Neumann, M., Treatment of Electrostatic Interactions in Computer Simulations and Calculation of Thermodynamic Properties Such as Free Energies and Pressures. In *Simulation and Theory of Electrostatic Interactions in Solution: Computational Chemistry, Biophysics, and Aqueous Solutions*, Pratt, L. R.; Hummer, G., Eds. 1999; Vol. 492, pp 84-103.
51. Asthagiri, D.; Pratt, L. R.; Ashbaugh, H. S. Absolute Hydration Free Energies of Ions, Ion-Water Clusters, and Quasichemical Theory. *J. Chem. Phys.* **2003**, *119*, 2702-2708.
52. Joung, I. S.; Cheatham, T. E. Molecular Dynamics Simulations of the Dynamic and Energetic Properties of Alkali and Halide Ions Using Water-Model-Specific Ion Parameters. *J. Phys. Chem. B* **2009**, *113*, 13279-13290.
53. Shi, W.; Maginn, E. J. Continuous Fractional Component Monte Carlo: An Adaptive Biasing Method for Open System Atomistic Simulations. *J. Chem. Theory Comput.* **2007**, *3*, 1451-1463.
54. Bratko, D.; Woodward, C. E.; Luzar, A. Charge Fluctuation in Reverse Micelles. *J. Chem. Phys.* **1991**, *95*, 5318-5326.
55. Chase, J., M. Thermochemical Tables. *J. Phys. Chem. Ref. Monograph ACS, AIP* **1998**.
56. Xu, B. X.; Qiao, Y.; Zhou, Q. L.; Chen, X. Effect of Electric Field on Liquid Infiltration into Hydrophobic Nanopores. *Langmuir* **2011**, *27*, 6349-6357.
57. Acharya, H.; Ranganathan, S.; Jamadagni, S. N.; Garde, S. Mapping Hydrophobicity at the Nanoscale: Applications to Heterogeneous Surfaces and Proteins. *Faraday Discuss.* **2010**, *146*, 353.
58. Patel, A. J.; Varilly, P.; Jamadagni, S. N.; Acharya, H.; Garde, S.; Chandler, D. Extended Surfaces Modulate Hydrophobic Interactions of Neighboring Solutes. *Proc. Natl. Acad. Sci. U. S. A.* **2011**, *108*, 17678-17683.

59. Bratko, D.; Daub, C. D.; Luzar, A. Field-Exposed Water in a Nanopore: Liquid or Vapour? *Phys. Chem. Chem. Phys.* **2008**, *10*, 6807-6813.
60. Gao, Z. H.; Giovambattista, N.; Sahin, O. Phase Diagram of Water Confined by Graphene. *Sci. Rep.* **2018**, *8*, 6228.
61. Daub, C. D.; Bratko, D.; Luzar, A. Nanoscale Wetting under Electric Field from Molecular Simulations. *Top. Curr. Chem.* **2012**, *307*, 155-179.
62. Cai, B. Y.; Yang, J. T.; Guo, T. M. Interfacial Tension of Hydrocarbon Plus Water/Brine Systems under High Pressure. *J. Chem. Eng Data* **1996**, *41*, 493-496.
63. Matubayasi, N.; Motomura, K.; Kaneshina, S.; Nakamura, M.; Matuura, R. Effect of Pressure on Interfacial Tension between Oil and Water. *Bull. Chem. Soc. Japan* **1977**, *50*, 523-524.
64. Horinek, D.; Netz, R. R. Specific Ion Adsorption at Hydrophobic Solid Surfaces. *Phys. Rev. Lett.* **2007**, *99*, 226104.
65. Luzar, A.; Svetina, S.; Zeks, B. The Contribution of Hydrogen-Bonds to the Surface-Tension of Water. *Chem. Phys. Lett.* **1983**, *96*, 485-490.



For Table of Contents Only